Numerical and Experimental Study of the Interaction of a Spark-Generated Bubble and a Vertical Wall[1]

Arvind Jayaprakash[2], Chao-Tsung Hsiao, and Georges Chahine

DYNAFLOW INC.
www.dynaflow-inc.com
Jessup, Maryland, USA

ABSTRACT

An understanding of the fundamental mechanisms involved in the interaction between bubbles and structures is of importance for many applications involving cavitation erosion.

Generally, the final stage of bubble collapse is associated with the formation of a high-speed reentrant liquid jet directed towards the solid surface. Local forces associated with the collapse of such bubbles can be very high and can exert significant loads on the materials. This formation and impact of liquid jet is an area of intense research. Under some conditions the presence of gravity and other nearby boundaries and free surfaces alters the jet direction and need to be understood, especially that in the laboratory, small scale tests in finite containers have these effects inherently present.

In this work, experiments and numerical simulations of the interaction between a vertical wall and a bubble are carried out using DYNAFLOW's three-dimensional code, 3DYNAFS-BEM©, which models the unsteady dynamics of a liquid flow including the presence of highly non-linear time evolving gas-liquid interfaces. The numerical predictions were validated using scaled experiments carried out using spark generated bubbles. These spark bubble tests produced high fidelity test data that properly scale the fluid dynamics as long as the geometric non-dimensional parameters, gravity and time are properly scaled. The use of a high speed camera allowing framing rates as high as 50,000 frames per second to photograph the bubbles produced high quality observations of bubble dynamics including clear visualizations of the reentrant jet formation inside the bubble. Such observations were very useful in developing and validating the numerical models. The cases studied showed very good correlation between

[1] *Originally presented as Paper IMECE 2010-40515 at ASME International Mechanical Engineering Congress & Exposition, Nov. 12-18, 2010, Vancouver, British Colombia, Canada [1].*

[2] *Corresponding author, Email: arvind@dynaflow-inc.com, Tel: 001-301-604-3688*

the numerical simulations and the experimental observations and allowed development of predictive rules for the re-entrant jet characteristics, including jet angle, jet speed, and various geometric characteristics of the jet.

NOMENCLATURE

α	Jet Angle
D_c	Bubble Center initial location from Free Surface
$\mathcal{F}$	Froude Number defined in (2)
$\mathcal{K}$	Jet Kinetic Energy
H	Jet Length
P_{amb}	Hydrostatic Pressure at the location of the bubble center
P_{atm}	Ambient Pressure above the Free Surface
P_v	Vapor Pressure of Ambient Liquid
P_{g0}	Bubble Initial Gas Pressure
R_0	Bubble Initial Radius
R_{max}	Bubble Maximum Radius
R_{base}	Jet Base Radius
$R_{j\text{-}eq}$	Radius of a Cylinder with same volume and length as the jet
ρ	Density of host Liquid
$\mathcal{S}$	Jet Shape Ratio defined in (19)
$\mathcal{V}$	Jet Volume
V_{tip}	Node Averaged Jet Velocity
V_{mom}	Kinetic Energy Averaged Jet Velocity defined in (21)
V_{kin}	Momentum Averaged Jet Velocity defined in (22)
X	Standoff Distance

1- INTRODUCTION

Prediction of cavitation erosion or impact forces from collapsing bubbles on propellers, ship structures, and in general on any structure subjected to bubble dynamics is of great interest to many industries. Approaches to the

problem have covered the whole spectrum of fundamental and applied numerical, analytical, and experimental studies. Fundamental studies provide great insight into the mechanisms at play, while more empirical engineering studies based on experimental observations, though imperfect; provide useful and practical rules, which help the designer and engineer, select a design or a material. A combined approach is required to advance significantly the field.

Although bubble dynamics including pulsation and migration due to buoyancy and interaction with a nearby structure has been investigated extensively, the three dimensional character of the phenomenon had thus far prevented the establishment of rules of thumb easy to use by the scientific community.

When a bubble nuclei encounter large negative pressure gradients in the liquid flow, they grow explosively and then, once in a high pressure region, they collapse violently generating shock waves and high impact dynamic pressures from reentrant jets due to boundary condition asymmetries nearby boundaries, and in presence of bubble-bubble interactions [2-3].

In the absence of gravity effects or nearby objects, the bubble remains spherical, and its volume oscillations can be predicted analytically. Rayleigh [4] analyzed the collapse of an empty spherical cavity of initial radius, R_{max} , and found the time the cavity requires to collapse was:

$$\tau_{collapse} = 0.915 R_{\max} \sqrt{\frac{\rho}{P_{amb}}}, \tag{1}$$

where ρ and P_{amb} are the density and initial pressure of the ambient fluid. This ideal bubble period is commonly used to normalize time in bubble dynamics studies under more real fluid conditions. The effects of vapor pressure, non-condensable gas, surface tension, and a time-varying ambient pressure were then included, to produce the Rayleigh-Plesset equation [4,5], the equation of the wall motion for an oscillating, collapsing, and rebounding spherical bubble in an imposed pressure field. For given conditions, the full dynamics of the bubble oscillations can be predicted from this equation. Using the unsteady Bernoulli equation, one can then predict the time evolution of the pressure in the liquid around the bubble.

In many practical applications involving bubble collapse near a solid structure, competition exists between the forces of gravity, those due to the presence of the nearby structure, and the presence of the water free surface. In such cases the bubble collapses asymmetrically, resulting in the development of a reentrant jet followed by a toroidal bubble formation [6-23]. This high speed reentering jets can be very damaging. The intensity of the reentrant jet, its direction, and the momentum it carries during its impact on the nearby structure depends on both the gravity force and the strength of attraction of the nearby structure.

In practical terms, the jet characteristics depend on the bubble size, the ambient pressure, the gravitational force and the bubble standoff distance from the structure. These are further discussed below.

a. Gravity Effects

The relative importance of the gravity effects on bubble dynamics can be characterized by the ratio of the pressure difference between the top and the bottom of the bubble, and the hydrostatic pressure driving the bubble collapse. The pressure difference between the top and the bottom of the bubble characterizes the forces deforming the bubble (moving it away from the spherical shape). The average pressure of the hydrostatic head around the bubble, which can be approximated by the hydrostatic pressure at the bubble 'center', drives spherical volume change. The actual force responsible for the 'strength' of the bubble collapse is the difference between the hydrostatic head at the location of the bubble center, P_{amb}, and the pressure inside the bubble when it is at its maximum volume, $P_{i,min}$. This internal pressure is the sum of the liquid vapor pressure, P_v, and the minimum pressure of the gas in the bubble, $P_{g,min}$. For strong bubble collapses, $P_{i,min}$ is so much smaller than the collapse driving pressure, that it can be neglected.

The Froude number, $\mathcal{F}$, can be expressed as:

$$\mathcal{F} = \frac{P_{atm} + \rho g D_c}{2\rho g R_{\max}}, \tag{2}$$

where D_c is the initial bubble center depth measured from the free surface, and P_{atm} is the pressure above the free surface. For scaled testing, P_{atm} can be modified (e.g., by pulling vacuum in the tank) in order to maintain the same value of $\mathcal{F}$ between the scaled test and the full scale, which could be either a much larger or a smaller bubble. This is a very important consideration in conducting scaled testing [25,28]. In laboratory setting, P_{atm} is equal to the

pressure imposed above the free surface in the container used in the experiment. R_{max} is the maximum radius the bubble would achieve at the considered ambient pressure *if it were in an infinite medium.*

For large values of the Froude number, the effect of gravity is weak, and the bubble remains almost spherical. For small Froude numbers, bubble distortion due to gravity is important. Changes in the Froude number when the other parameters are kept constant illustrate the effect of the acceleration of gravity on the results. Very far from the walls the effect of the Froude number (i.e. gravity effects) are predominant. In that case the reentrant jet is directed 180° upwards. Very close to the wall, wall effects are predominant and the reentrant jet is directed at 90°, i.e. perpendicular to the wall. Near the wall, when the Froude number significantly decreases, i.e. shallow depth or very large bubble, wall and gravity effects compete, resulting in an angled jet, $180 < \alpha < 90$ towards the wall [30].

b. Standoff Effects

The non-dimensional parameter, χ, characterizing bubble-wall interaction problems is the ratio of the standoff distance, X, between the bubble center and the wall and the bubble maximum radius, R_{max}, the bubble would achieve if it was in an infinite medium [10-14]:

$$\chi = \frac{X}{R_{\max}}. \tag{3}$$

c. Objectives

To better understand the dynamics of a bubble collapsing near a structure and to easily quantify the reentrant jet dynamics, a canonical set-up with a single gas bubble near a vertical wall is selected for investigation. The sketch of the geometry along with the parameters involved is shown in Figure 1. As introduced in the previous section, the critical parameters involved in this set-up are the bubble size, its depth, the ambient pressure, and the bubble standoff distance from the structure.

The objectives of the combined numerical and experimental study are as follows:

a. Investigate the dynamics of bubble growth and collapse near a vertical rigid structure by performing simulations encompassing a wide range of cases.

b. Characterize the resulting reentrant jet.

c. Conduct scaled experiments to provide confidence in the numerical simulations.

d. Test the validity of the scaled experiments.

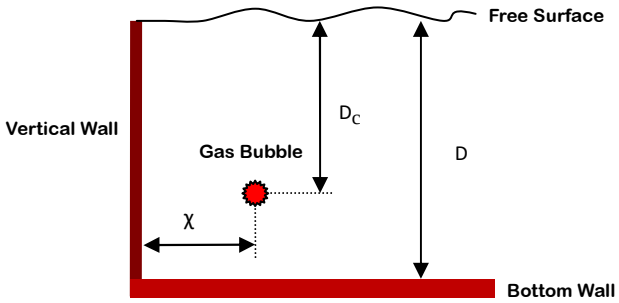

Figure 1. Definition sketch of the parameters of the problem of a bubble dynamics near a vertical wall, a free surface, and a rigid bottom.

2- NUMERICAL MODEL

The present numerical study is based on the Boundary Element Method (BEM) and uses the BEM module of the 3DYNAFS© code developed by DYNAFLOW, INC. [29-37].

For cavitation bubbles in water-like liquids, it is generally accepted that the viscous effects can be neglected during a bubble cycle and one can consider the fluid flow field as potential [32,33]. In addition if the liquid starts from rest the assumption of irrotational flow allows the definition of a velocity potential, ϕ:

$$\mathbf{u} = \Delta\phi, \tag{4}$$

where **u** is the velocity vector. The assumption that the liquid is incompressible leads to the Laplace equation for the potential:

$$\Delta^2\phi(\mathbf{x},t) = 0, \quad \mathbf{x} \in D, \tag{5}$$

where **x** is the spatial variable and *t* is time. On any free surface, e.g. the bubble surface S_b, of local normal, **n**, ϕ satisfies the kinematic boundary condition, which expresses equality between the fluid and the free surface normal velocities:

$$\frac{d\mathbf{x}}{dt} \cdot \mathbf{n} = \nabla\phi \cdot \mathbf{n}, \quad x \in S_b, \tag{6}$$

and the dynamic boundary condition:

$$\frac{\partial\phi}{\partial t} = -\frac{1}{2}\left|\nabla\phi\right|^2 + \frac{P_{amb} - P_b}{\rho}. \tag{7}$$

P_{amb} is the hydrostatic pressure at the point of initiation of the explosion, and $P_b(x,t)$ is the local pressure in the liquid at the bubble interface, ρ is the liquid density, and *t* is time.

The pressure can then be determined by integrating the momentum equation at any point within the liquid between this point and far from the bubble using Bernoulli's equation:

$$p(t) = P_{amb} - \rho\left[\frac{\partial\phi}{\partial t} + \frac{1}{2}\Delta\phi \cdot \Delta\phi\right]. \tag{8}$$

3- BUBBLE DYNAMICS MODEL

The pressure inside the bubble is assumed spatially homogeneous and the bubble content is assumed to be composed of both vapor of the liquid and non-condensable gas. The pressure at any instant is given by the sum of the partial pressures of the liquid vapor and of the non-condensable gases.

At normal ambient temperature, vaporization of the liquid occurs at a fast enough rates so that the vapor pressure inside the bubble, P_v , remains constant and equal to the equilibrium liquid vapor pressure at the ambient temperature. On the other hand, gas diffusion characteristic time is much longer than the bubble collapse characteristic time, so that the non-condensable gas of pressure, P_g, can be assumed to satisfy the polytrophic law,

$$P_g \mathcal{V}^k = \text{constant}, \tag{9}$$

where $\mathcal{V}(t)$ is the volume of the bubble at time *t*, and *k* is the polytropic exponent. This leads to the following form of the normal stress boundary condition at the bubble-liquid interface:

$$P_l = P_v + P_{go}\left[\frac{\mathcal{V}o}{\mathcal{V}}\right]^k - \sigma\mathcal{C}, \tag{10}$$

where P_{go} is the initial gas pressure in the bubble, and $\mathcal{V}_o$ is the initial volume of the bubble. The variable σ is the surface tension coefficient, and $\mathcal{C}$ is the local surface curvature given by

$$\mathcal{C} = \nabla \cdot \mathbf{n}\,. \tag{11}$$

The local normal **n** at the surface is defined by:

$$\mathbf{n} = \pm\frac{\nabla f}{\left|\nabla f\right|}, \tag{12}$$

where *f* is a local description of the surface. The appropriate sign is chosen so that all bubble surface normals point toward the liquid domain.

In addition to the boundary conditions on free surfaces, (6) and (7), the boundary conditions on any nearby solid body $\mathcal{S}_t$ are given by:

$$\frac{\partial\phi}{\partial n} = u_{n,} \qquad x \in \mathcal{S}_t, \tag{13}$$

where, u_n is the local normal velocity of the body in response to the bubble loading. u_n = 0 for a rigid wall.

At infinity, the fluid velocities due to the bubble dynamics vanish, and the boundary condition is

$$\lim\Big|_{x\to\infty}\left|\nabla\phi\right| = 0. \tag{14}$$

To complete the description of the problem, appropriate initial conditions are required. In earlier phases of our effort we had developed a method for determining these [6,7]. Briefly, the bubble dynamics at the initiation of the computation is assumed to be that of a the spherical bubble in a free field and the corresponding initial gas pressure is computed.

Thus, a closed system of equations is obtained to solve for ϕ both in space and time. Given the conditions (6) through (14), Laplace's equation (5) can be solved and an updated shape of the bubble surface and new values of ϕ on the surface can be obtained by integrating (6) and (7) with respect to time.

a. Boundary Element Equation Representation

The initial-boundary value problem of Laplace's equation for velocity potential ϕ is solved by the Boundary Element Method, which is based on an integral solution of the Laplace equation using Green's theorem. This can be written in the following form:

$$\iiint_{\mathcal{D}} \left(\phi \nabla^2 G - G \nabla^2 \phi\right) d\mathcal{D} = \iint_{\mathcal{S}} \left(\phi \nabla G - G \nabla \phi\right) \cdot n d\mathcal{S}. \tag{15}$$

In this expression $\mathcal{D}$ is the domain of integration of elementary volume d$\mathcal{D}$. The boundary surface of $\mathcal{D}$ is S with elementary surface element d$\mathcal{S}$ and local normal unit vector **n**. The variable ϕ is the flow velocity potential, harmonic in the fluid domain D, and *G* is Green's function. If *G* is selected to be harmonic everywhere but at some discrete points, Equation (15) simplifies considerably. For instance, if P is a fixed point and M is a field point and we select

$$G = \frac{1}{\left|\overrightarrow{MP}\right|}, \tag{16}$$

Equation (15) reduces to Green's formula:

$$\alpha\pi\phi\left(P\right) = \iint_{\mathcal{S}} \left\{ -\frac{\partial \phi}{\partial n} \frac{1}{\left|\overrightarrow{MP}\right|} + \phi \frac{\partial}{\partial n} \left(\frac{1}{\left|\overrightarrow{MP}\right|} \right) \right\} d\mathcal{S}. \tag{17}$$

$\alpha\pi$ is the solid angle from which P locally "sees" the domain D.

- $\alpha = 4$, if P is a point in the fluid,

- $\alpha = 2$, if P is a point on a smooth surface, and

- $\alpha < 4$, if P is a point at a sharp corner of the discretized surface.

This equation states that if the velocity potential ϕ and its normal derivatives are known on the boundary surface $\mathcal{S}$ of a domain $\mathcal{D}$, then ϕ can be determined anywhere in $\mathcal{D}$ by integration over the boundary surface. Using this expression the Boundary Element Method reduces by one the dimension of the problem of solving the Laplace equation.

The main idea is to incorporate Equation (17) into a time stepping procedure. For instance, if we restrict ourselves to points P on the surface, Equation (17) provides a relationship between ϕ and $\partial\phi / \partial n$ on that surface. Now if either of these two variables (e.g., ϕ) is known everywhere on the surface at a given time step, Equation (17) enables one to determine the other variable (e.g., $\partial\phi / \partial n$) at that time step. One can then use the knowledge of $\partial\phi / \partial n$, the normal velocity to the surface, to update the position of the surface. Knowing the velocity vector and the velocity potential at each point and applying the unsteady Bernoulli equation, one obtains $\partial\phi / \partial t$ and deduces from it the value of ϕ at the next time step. This provides a numerical time-stepping procedure to describe the time evolutions of $\partial\phi / \partial n$ and the bubble surface.

b. Jet Characterization

An important portion of the impact load on a nearby material following the growth and collapse of the gas/vapor cavity is directly dependent on the energy contained in the impacting reentrant jet formed at the end of the cavity collapse. It is therefore essential to be able to accurately characterize the reentrant jet.

1. Jet Detection

The 3DYNAFS© code contains schemes for detecting reentrant jet formation and for computing the various jet characteristics. The detection is based on the geometric shape of the bubble-liquid interface, and can either be turned on during the computation of the bubble dynamics, or used in post-processing after the completion of the computations. In both cases, the schemes recognize the bubble collapse stage as a decrease in the bubble volume,

and then proceed to detecting the point where the bubble surface becomes concave (mathematically, when the curvature become negative) and has the maximum normal velocity.

2. Jet Geometry

The jet geometry can be characterized in several ways. For the analysis presented here, five main geometric quantities were selected as in [2,3,32] and used for comparing jet characteristics:

- Jet width, W
- Jet base radius, R_{base}
- Jet length, H
- Jet equivalent cylinder radius, $R_{j\text{-}eq}$
- Shape factor, S
- Jet direction, α

In order to define the jet quantities, we consider the '*jet base plane*' as that being defined by a plane perpendicular to the jet direction and tangent to the bubble surface on the jet side. The jet volume is defined as the volume of the liquid contained between the *'jet base plane'* and the jet tip. The jet angle is the angle that the jet axis makes with the vertical *Z* coordinate axis. The schematic of the jet quantities are shown in Figure 2.

3. Jet Equivalent Cylindrical Radius and Shape Factor

The jet equivalent cylindrical radius, $R_{j\text{-}eq}$, is defined using the jet volume, $\mathcal{V}_j$, and the jet length, H. It is the radius of a cylindrical slug with the same volume as the reentrant jet volume. Its expression is thus given by:

$$R_{j-eq} = \sqrt{\frac{\mathcal{V}_j}{\pi H}}. \tag{18}$$

The shape factor expresses how different is the reentrant jet from a cylindrical slug, and is defined as the ratio between the equivalent radius and the jet base radius of diameter, W.

$$S = \frac{R_{j-eq}}{R_{base}} = \frac{2R_{j-eq}}{W}, \tag{19}$$

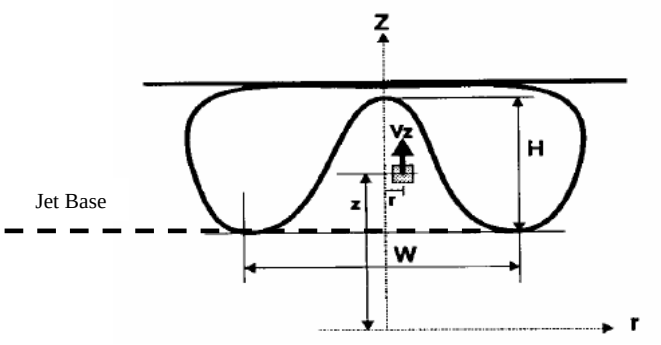

Figure 2. Quantities used to characterize a collapsing bubble reentrant jet.

4. Reentrant Jet Velocities and Angles

Defining the jet velocity vector as being that of the fastest node in the jet region (V_{tip}) has two major deficiencies:

a) it gives over-estimated values for the jet velocities that do not correlate with the loading on the material.

b) it is sensitive to the computation method, and to numerical errors and instabilities.

To better characterize the reentrant jet, we introduce the following three 'average *jet velocity'* definitions.

5. Jet Tip Average Velocity and Direction

The geometric average *jet tip velocity* improves over using the highest node velocity by averaging the vector velocities in the tip region using the fastest node and all surrounding nodes in the discretized bubble shape. This value is still an over-estimate but could characterize well the impact pressures at the moment of jet impact on the obstacle.

Two other quantities suffer much less from the above problems and better account for the characteristics of the overall jet rather than those of the jet tip region, and are presented below.

6. Momentum Averaged Jet Velocity and Direction

The '*momentum averaged jet velocity'* is based on a computation of the momentum of the reentrant jet and has the following definition:

$$\mathbf{V}_{mom} = \frac{1}{\mathscr{V}} \int_{\mathscr{V}} |\mathbf{V}| \, d\mathscr{V}. \tag{20}$$

where $\mathbf{V}$ is the vector fluid velocity at any point in the jet volume, $\mathcal{V}$. The magnitude of $\mathbf{V}_{mom}$ is the '*momentum averaged velocity*' while the direction defines the orientation of the averaged jet velocity with respect to the axis coordinates.

7. Energy Averaged Jet Velocity

The kinetic energy, $\mathcal{K}$, contained within the fluid in the jet volume, $\mathcal{V}$, can be defined as follows:

$$\mathcal{K} = \int_{\mathcal{V}} |\mathbf{V}|^2 \rho d\mathcal{V}. \tag{21}$$

We also defined $\bar{V}_{kin}$ as the '*kinetic energy averaged jet velocity*' given by:

$$\bar{V}_{kin} = \frac{1}{\mathcal{V}} \sqrt{\int_{\mathcal{V}} |\mathbf{V}|^2 d\mathcal{V}}. \tag{22}$$

C. A Typical 3DynaFS_Bem Simulation

To introduce the analysis presented below and illustrate a typical behavior of a bubble growing and collapsing near a vertical structure we consider a bubble of initial radius 0.1 mm, initially centered 6 cm below the free surface and 0.85 cm away from the vertical wall. The water depth in the tank is 12 cm, the pressure above the free surface is 12200 Pa, the initial gas pressure in the bubble is 6.6 x10^9 Pa, and the gas compression law constant is *k=1.25*.

Figure 3 show bubble contour time sequences of a crosscut through the bubble in the plane of symmetry perpendicular to the wall. The figure shows a cut in the diametrical plane x = 0, perpendicular to the wall, at increasing time instants of the simulation. The contours are printed out at constant time step intervals and not times. Since the code uses adaptive time stepping, the time steps become smaller and smaller as the collapse accelerates and this is aimed at capturing better the dynamics. The vertical red lines indicate the position of the vertical wall. The left half of Figure 3 shows the bubble during its growth phase, while the right half shows the bubble during its collapse. The contours during growth show that the bubble remains spherical but in the region close to the wall, where the bubble squeezes against the rigid wall. During the collapse the part of the bubble far from the wall

collapses much faster than the rest of the bubble as the liquid pressure in that region exceeds the other pressures due to the asymmetry created by the presence of the wall. The dynamics ends up producing a reentrant jet that penetrates the bubble, until hitting the other side of the bubble and then ultimately the nearby rigid wall.

Figure 4 through Figure 6 present the output of the computations illustrating the non-dimensional jet characteristics for the case of Figure 3. Figure 4 shows the non-dimensional time variations of the geometric characteristics of the reentrant jet: the jet length, the jet base and the jet equivalent cylindrical radius. We can see that all three jet quantities increase with time in this case as the jet advances through the bubbles.

The jet geometric characteristics and the various jet reentrant speeds as a function of time, all normalized as follows:

- Lengths are normalized by the bubble maximum radius, R_{max}
- Times are normalized by the bubble Rayleigh time: $T_{Ray} = R_{\max}\sqrt{\dfrac{\rho}{P_{amb} - p_v}}$
- Velocities are normalized by:

  $V_{char} = R_{\max} \,/\, T_{Ray} = \sqrt{\dfrac{P_{amb} - p_v}{\rho}}$, where P_{amb} is the hydrostatic pressure at the location of the bubble center and P_v is the liquid vapor pressure.

Figure 5 shows the shape ratios are plotted as functions of time. We notice that the jet shape ratio, characterizing the jet, remains practically constant during the jet dynamics, and fluctuates near 0.5. The jet length, on the other hand as seen in Figure 4, increases monotonously until touchdown.

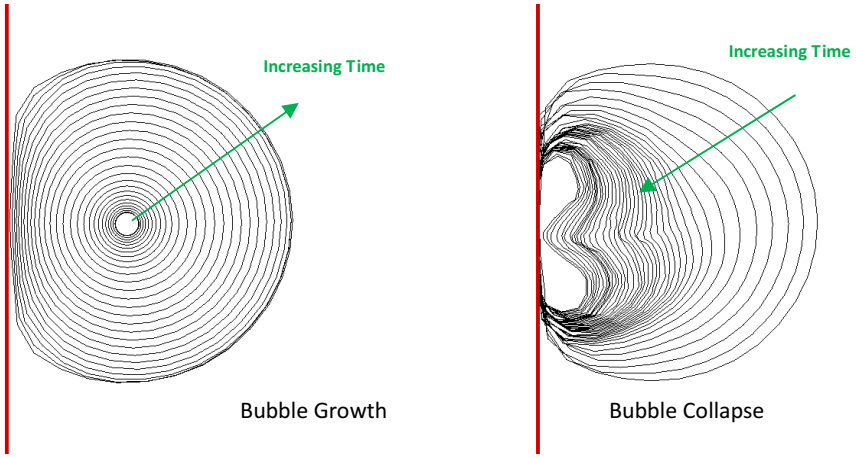

Figure 3. Evolution of the bubble diametrical contours. The left panel shows a bubble growth sequence, while the right panel shows bubble collapse and reentrant jet formation. Contours are shown a regular time step intervals not equal times (time steps are very much reduced during the bubble collapse period). The bubble initial center is at a depth of 12 cm, the tank pressure over the free surface is 12,200 Pa, the initial gas pressure is 6.6×10^{9} Pa, and the initial bubble radius is 0.1 mm.

Figure 6 shows the jet velocities as functions of time. We can observe that all three plotted velocities increase in time as the bubble collapse proceeds. It can be seen that the tip velocity is higher than the tip averaged velocity and the velocities based on the momentum and kinetic energy, and, not as smooth in comparison. This is expected since these are geometrically averaged value, with the jet speed inside the reentrant jet decreasing away from the jet tip. The fluctuations in the monitored jet parameters, as can be seen in Figure 4, Figure 5 and Figure 6 are due to the fact that regridding is applied to the 3D surface to maintain good grid distribution, and to the fact that the fastest node (around which the jet is assumed to evolve) may change during the computations from one time step to another. The fluctuations are left in the figure and are not smoothed out to show the degree of accuracy of the results.

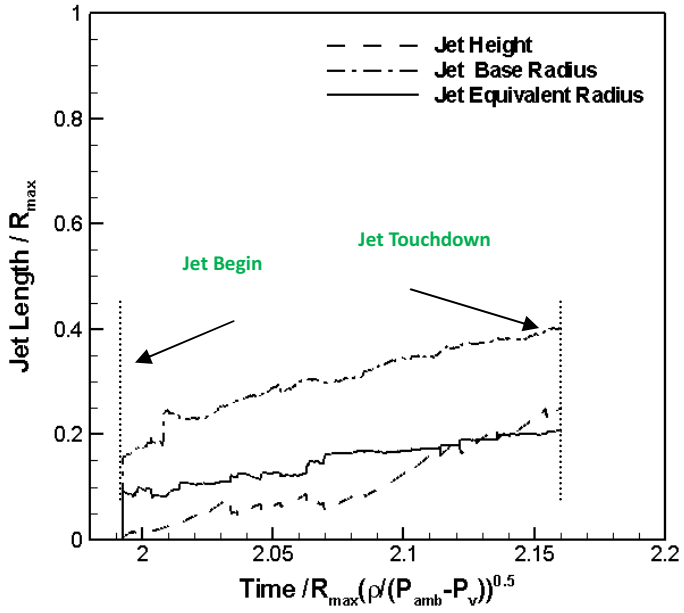

Figure 4. Normalized reentrant jet dimensions as a function of time for the bubble of Figure 3.

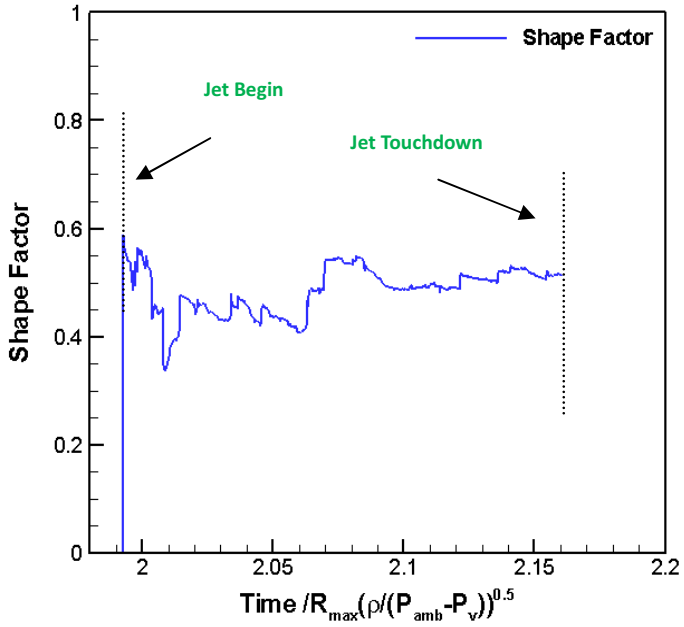

Figure 5. Normalized reentrant jet shape factor for the bubble of Figure 3.

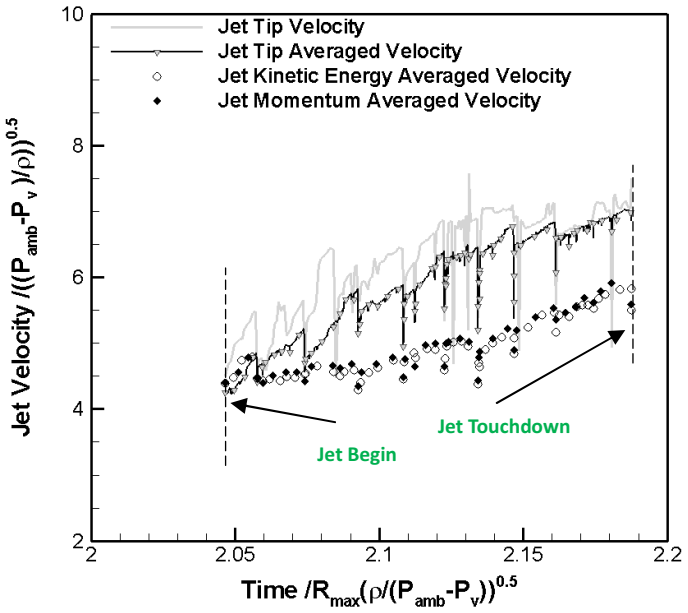

Figure 6. Normalized jet speed as a function of time. Various definitions of the jet as described in the text above, Eq.(20) - (22). Same conditions as bubble in Figure 3.

Case	3DynaFS-BEM Simulations			
	Bubble Initial Radii [R_0]	Bubble Initial Gas Pressure [P_{g0}]	Stand-off Distance [χ]	Froude Number [F]
	cm	MPa	R_{max}	-
1	1.17	83.4	0.25	33.6
2	1.17	83.4	0.50	33.6
3	1.17	83.4	0.75	33.6
4	1.17	83.4	1.00	33.6
5	1.17	83.4	1.25	33.6
6	1.17	83.4	1.50	33.6
7	1.17	83.4	2.00	33.6

Table 1. List of 3DynaFS©-BEM Simulation Parameter. Only the stand-off distance is varied for this study. However, the Froude Number is the same as in the experiment and its variations have been considered elsewhere.

d. Simulation Matrix

A set of simulations were conducted to characterize the bubble dynamics and the resulting reentrant jet parameters defined earlier. Table 1 shows the simulation matrix conducted to investigate the jet parameters. The spark test will then try to conserve the values of the non-dimensional parameters and validate the numerical results.

4- EXPERIMENTAL SET-UP

An effective method to study bubble/wall interaction is the use of electric spark generated bubbles in a container where the ambient pressure can be controlled. Spark generators have been used for studying bubbles in a liquid for quite a long time [7-26]. DYNAFLOW, INC. has several test chambers that can be used to simulate full-scale bubble dynamics, and is equipped with flow diagnostics tools including high speed photography and pressure measurement capabilities. Spark bubble tests produce high fidelity test data that properly scale the fluid dynamics corresponding to the actual scale conditions.

Scaling is conducted by conserving the Froude Number and the details of the geometric configuration defined by the non-dimensional geometric parameters. The use of high speed cameras to photograph spark-generated bubbles produces high quality observations of bubble dynamics including clear visualizations of reentrant jet formation inside the bubble.

a. Spark Bubbles Generation

Spark bubbles are generated by the underwater discharge between two coaxial electrodes within a transparent cell of a high-voltage charge stored in capacitors contained. The underwater spark discharge is a process by which electrical energy is converted into small volume plasma which has temperatures as high as 20,000^{o}K, and pressures as high as 10^{9} Pascals [7]. As the trigger pulse breaks down the hold-off gap between electrodes, current flows between the electrodes with energy being absorbed in the plasma at a rate depending upon the power input and the inertia of the water. Eventually, due to a decrease in the voltage and an increase in the ionization, temperature, and pressure of the plasma, the spark is extinguished. The energy is initially stored in the plasma in the form of dissociation, excitation, ionization, and kinetic energy of the constituent particles. While the heated and pressurized plasma will tend to expand, the inertia of the outside water will tend to confine it. Mechanical work, light radiation, thermal radiation, and thermal conduction dissipate the energy from the plasma at a rate slower than energy input from the spark [7].

Because of the high pressure, the liquid near the plasma interface is initially compressed. This high pressure leads to the formation of a shock wave that radiates outward. The energy in the shock wave comprises 20 to 50 percent of the energy imparted by the spark into the water [7]. After emission of the shock wave, the pressure in the gas sphere quickly falls, but remains well above that of the surrounding liquid. The pressure difference, however, is small enough that compressible effects can be neglected. From this point on, incompressible hydrodynamic effects dominate. The pressurized gas expands into a large bubble which subsequently collapses and re-expands. The phenomena preceding the incompressible hydrodynamic phase occur quickly and are accompanied by light generation that prevents accurate determination of the initial bubble radius using conventional high-speed photography.

b. Spark Bubbles Tests

The Froude number, defined in (2), is conserved between the actual scale bubble and the spark generated bubble by controlling the pressure above the free surface in the test cell. Modifying the value of P_{cell} affects the Froude Number not only through the numerator of Equation (2), but also through R_{max} in the denominator, which increases when P_{cell} is lowered.

The energy of the bubble is controlled by adjusting the voltage supplied to the capacitor of the spark generator. In cases where the bubble is significantly distant from boundaries, it retains an almost spherical shape through the time of its maximum volume and a sphere radius could be easily measured. In cases where the bubble is distorted by the presence of boundaries, an equivalent radius can be used. Here, it was obtained for each case by assuming the bubble to be axisymmetric, and calculating its volume as the volume of a solid of revolution of the observed outline around its vertical axis.

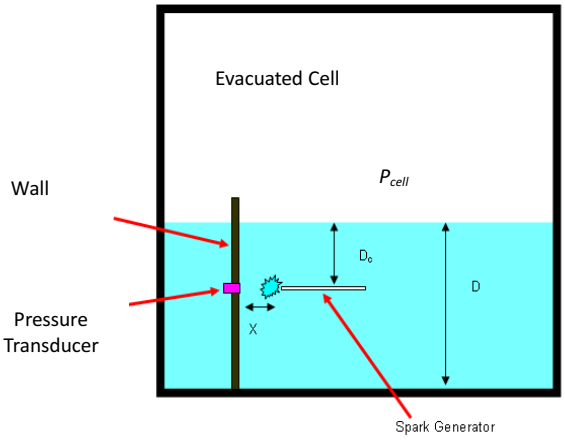

Figure 7. Schematic of a DYNAFLOW spark cell set-up for single and multiple bubble dynamics study.

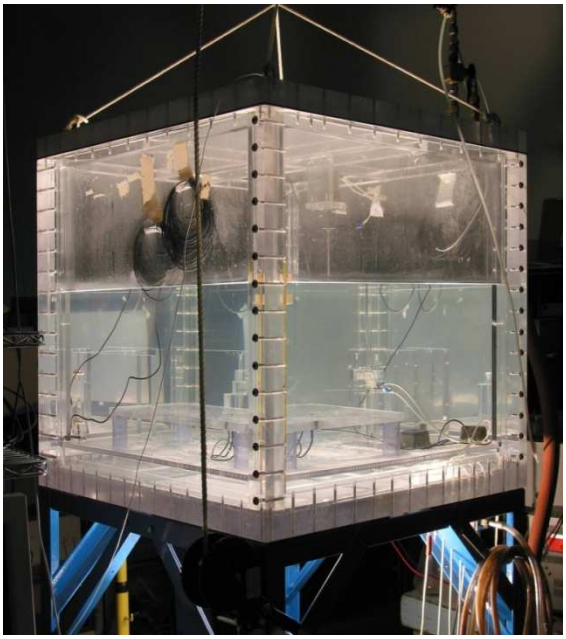

Figure 8. A picture of the large DYNAFLOW's spark-generated bubbles test facility. The Plexiglas tank dimensions are 1m x 1m x 1m and the wall thickness is 2.5 cm. The tank can support internal pressure as low as 3,500 Pa.

The ambient pressure was calculated based on the measured ambient pressure in the vacuum cell and the hydrostatic head measured using the depth of the electrodes, and the vapor pressure was deduced from the ambient water temperature.

The transparent walls allowed recording of the bubble dynamics by a high-speed digital camera (Redlake Imaging model PCI8000S). The tanks can be equipped with high frequency response hydrophones and transducers, which can be used to measure the pressures in the liquid and at the walls of nearby structures [28,40].

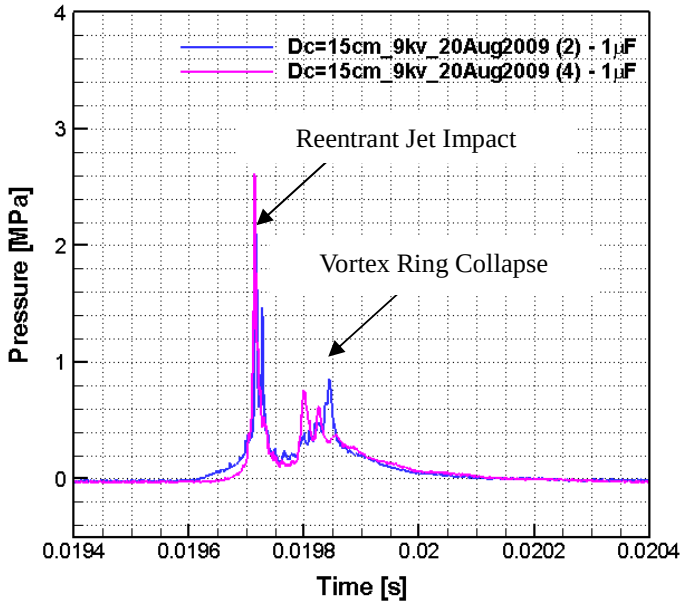

Figure 9. Pressures recorded on the rigid wall at the end of the bubble collapse for two repeated runs. The experimental conditions are: Electrode depth of 15 cm from free surface; 1.7 cm from the vertical wall, bottom depth of 24 cm, and cell pressure of 7270 Pa.

Pressure measurements at the wall are illustrated in Figure 9 , which shows the pressure recorded at the time of bubble touchdown with a PCB-101A03 transducer flush mounted on the wall at the same depth of the initial bubble center. The pressure signals indicate the presence of two peaks at collapse, one corresponding to the reentrant jet impact and the other corresponding to the collapse of the remaining vortex ring. Depending upon the stand-off distance the amplitude of the two peaks varies. We are in the process of modeling these phenomena and we will discuss this in detail in subsequent publications.

5- RESULTS AND DISCUSSION

For this study, three sets of each of the scaled spark tests were conducted using the spark tank. The lists of experiments are tabulated in Table 2.

a. *Validation of the code*

Using image analysis techniques, the bubble outlines were extracted from the recorded high-speed movies of the spark tests. Then the volume of the bubble was computed as the volume of a solid revolution of the observed outline around its horizontal axis. Finally, the bubble equivalent radii were deduced from the computed volume.

Case		Spark Test Parameters			
	Electrode Depth	Bottom Depth	R_{max}	Stand-Off	Froude No.
	(cm)	(cm)	(cm)	(cm)	(F)
1	6	12	1.35	0.25	33
2	6	12	1.35	0.60	33
3	6	12	1.35	0.85	33
4	6	12	1.35	1.00	33
5	6	12	1.35	2.00	33

Table 2. List of scaled spark test parameters used in this study. The pressure in the cell was maintained at 12,200 Pa and the spark energy was maintained the same.

Presented in Figure 11 through Figure 13 are two examples from the high-speed movies, 3DYNAFS© results and their corresponding bubble equivalent radii evolution computed using image analysis techniques. The snapshots correspond the time of bubble reaching its maximum radius and at touchdown.

The scaled spark experiments were also used to provide confidence in the numerical simulations. In order to test the validity of using 3DYNAFS-BEM© for real-scale studies and to prove the valid usage of laboratory scale experiments to study real-scale bubble near a vertical structure, matching 3DYNAFS Simulations were carried out.

Initial conditions for the 3DYNAFS-BEM© runs (initial radius and gas pressure required to recover the spark energy), were provided by simulations runs carried out with the PHANTOMCLOUD module of 3DYNAFS© to match the equivalent bubble radii obtained from the image analysis of the high-speed movies when the bubble is far from boundaries.

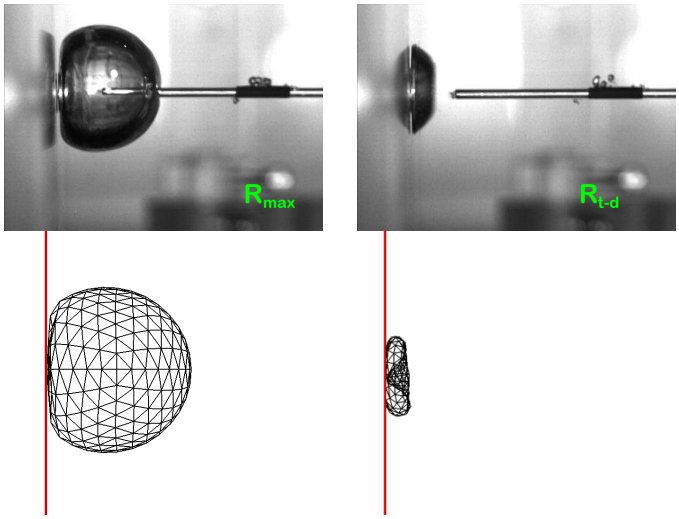

Figure 10. Snapshots of spark bubble and corresponding 3DYNAFS© bubble for the electrode depth of 6 cm from free surface; 0.85 cm from simulated wall, depth of 12 cm, and cell pressure of 12,200Pa. The non-dimensional stand-off χ = 0.65 R_{max}.

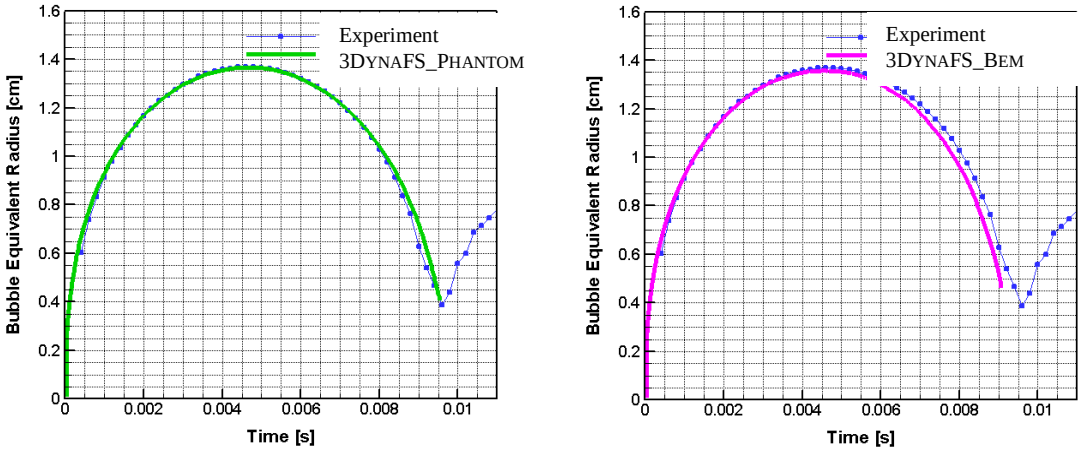

Figure 11. Comparison of the evolution of the bubble equivalent radii between scaled spark tests and corresponding 3DYNAFS©-PHANTOMCLOUD and 3DYNAFS©-BEM simulations using R_0= 0.04 cm, R_{max}= 1.38 cm and P_{atm} = 12200 Pa. This corresponds to the conditions of Figure 10.

Shown in Figure 10 through Figure 13 are comparisons of spark generated bubble pictures selected from high speed movies and the corresponding 3DYNAFS-BEM© bubble shape for selected cases from those tabulated in Table 2. The resulting bubble equivalent radii predictions from 3DYNAFS-BEM© simulations show very good match with the experiments and validate use of the 3DYNAFS© code.

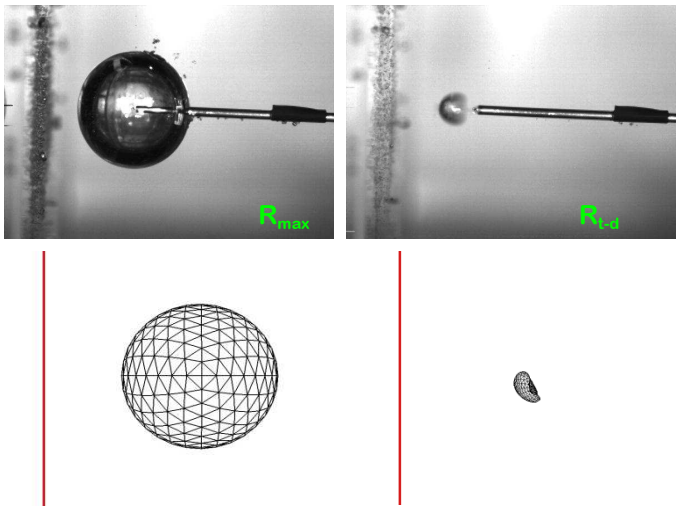

Figure 12. Snapshots of spark bubble and corresponding 3DYNAFS© bubble for the electrode depth of 6 cm from free surface; 2 cm from simulated wall, depth of 12 cm, and cell pressure of 12,200Pa. The non-dimensional stand-off χ = 1.5 R_{max}.

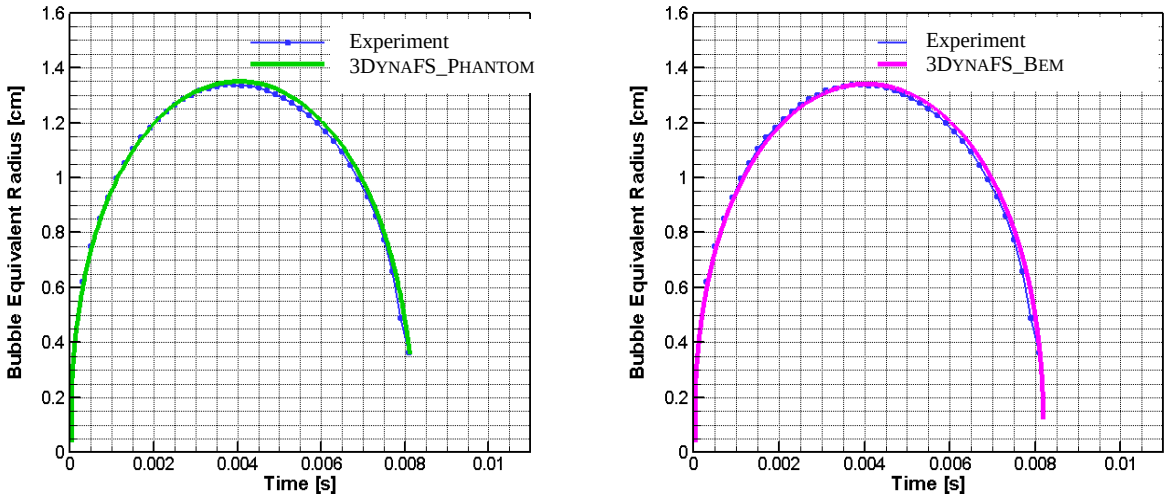

Figure 13. Comparison of the evolution of the bubble equivalent radius between scaled spark tests and corresponding 3DYNAFS-PHANTOMCLOUD© and 3DYNAFS-BEM© simulations using R_0= 0.04 cm, R_{max}= 1.35 cm and P_{atm} = 12500 Pa. This corresponds to the conditions of Figure 12.

b. Influence of the Wall Standoff

To understand the influence of bubble stand-off on the reentrant jet dynamics, 3DYNAFS-BEM© simulations with varying standoffs were also carried out. Shown in Figure 14 are the x=0 plane cross-cuts for the various cases.

From these cross-cuts, we can qualitatively observe that, for the cases with standoffs larger than the bubble maximum radius, the bubble collapses to a much smaller volume before touchdown than that of the cases with standoffs smaller than the bubble maximum radius. Also when moving away from the wall, where the reentrant jet is almost perpendicular to the wall, the direction of the jet becomes much more sensitive to gravity and the presence of the bottom and the free surface.

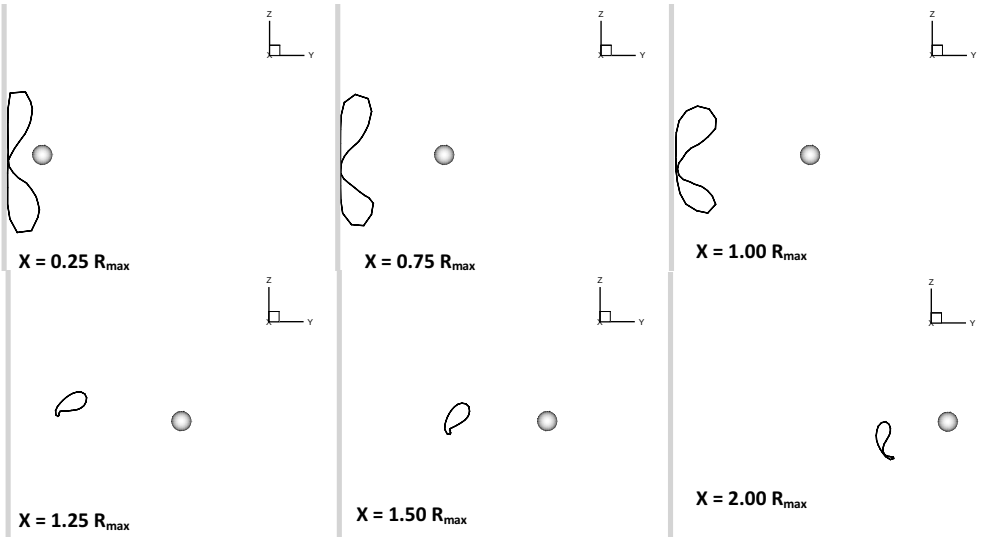

Figure 14. Cross-cut of bubble shape at touchdown for various stand-off distances from the wall. The simulation conditions are: R_0= 1.17 cm, R_{max}= 16.48 cm, D = 121.92 cm and P_{atm} = 101,230 Pa. Also shown are the bubble initial locations.

Further quantitative non-dimensional jet parameters variations of spark bubbles versus stand-off are shown in Figure 15 through Figure 18, reaffirm a strong dependence on standoff, especially, for the range of interest to this study when the standoffs are smaller than the bubble maximum radius (most damaging cases). The larger standoffs have been discussed in previous publications and asymptotic behaviors were described [11,12,25].

c. Jet Characteristics Variations with Standoff

Figure 15 show the jet angle as a function of the standoff distance from the vertical wall, while all other quantities are conserved. For the Froude number of interest to this study, close to the wall, wall effects are predominant and the reentrant jet is directed at almost 90°, i.e. perpendicular to the wall. When the Froude number

significantly decreases, i.e. shallow depth or very large bubble, wall and gravity effects compete, resulting in an angled jet, $180 < \alpha < 90$ towards the wall. One has however to note that far from the wall for the conditions presented here the reentrant jet could be very shallow and almost tangential to the bubble side (see Figure 14) and this makes the determination of the angle imprecise both numerically and experimentally.

Figure 16 show the normalized reentrant jet equivalent radius, base radius, and jet height as a function of standoff distance. Figure 16 further corroborates the fact that for the cases with larger standoffs, the reentrant jet almost does not occur and the base radius at touchdown is very small, which is a result of the bubble collapsing to a smaller volume than that of the cases with standoffs less than the bubble maximum radius. At the standoff less than R_{max} the reentrant jet is well defined and its normalized base radius and well as the equivalent radius are about twice those at the larger than R_{max}. These dimensions then does not vary significantly when χ is reduced below 1. The jet height on the other hand is more sensitive to the standoff and as a result reflects much better the volume contained in the reentrant jet as shown next.

Figure 17 shows the normalized jet volume as a function of standoff distance. For standoff distances larger than one the jet volume is negligible and explains the lack of interest in that region of the variable space. For distances less than one, the volume goes through a maximum when the standoff is between 0.5 and 1. Measurements and numerical evaluations of the jet volume are however more sensitive to errors and this explain some discrepancy between experiments and numerical results.

Figure 18 shows the average jet velocity as a function of standoff distance. Here the effect of the standoff is very significant. The average jet velocity increases significantly for standoffs larger than R_{max}, as the bubbles with larger standoffs collapse to smaller sizes before touchdown, the jet (if it develops) has enough time and distance to accelerate to a larger velocity magnitude. This is however misleading as this jet develops far from the wall, contains very little momentum because of its small volumes as we will see below and very little of its energy can be transferred to the wall. For standoffs below R_{max}, the reentrant jet speed at time of touchdown continues to decline as the jet has less and less time to develop and thus to achieve a large value. A blow up of this region of interest is

shown in Figure 18 (Right), which illustrates that the momentum averaged jet velocity normalized with the characteristic velocity scale, $\sqrt{\frac{P_{amb} - p_v}{\rho}}$ decays from 9 to 6 as the standoff varies from R_{max} to R_{max} /4.

The picture is however not complete if we do not consider the energy contained in the advancing jet, i.e. consider both speed and mass of the liquid contained in the jet. Figure 19 show the jet momentum normalized by $\rho R_{\max}^3 \sqrt{\frac{P_{amb} - p_v}{\rho}}$. As we can see there is an optimum standoff distance value to maximize the momentum since the normalization is the same for all case as a function of standoff distance. This quantity clearly establishes a region of maximum available jet momentum between standoffs 0.75 R_{max} and R_{max}, having potential for maximum damage. In all cases, one has to remember that if the jet does not directly hit the wall and has to cross a liquid layer before reaching the wall, damping of the jet will reduce the actual momentum transferred to the wall.

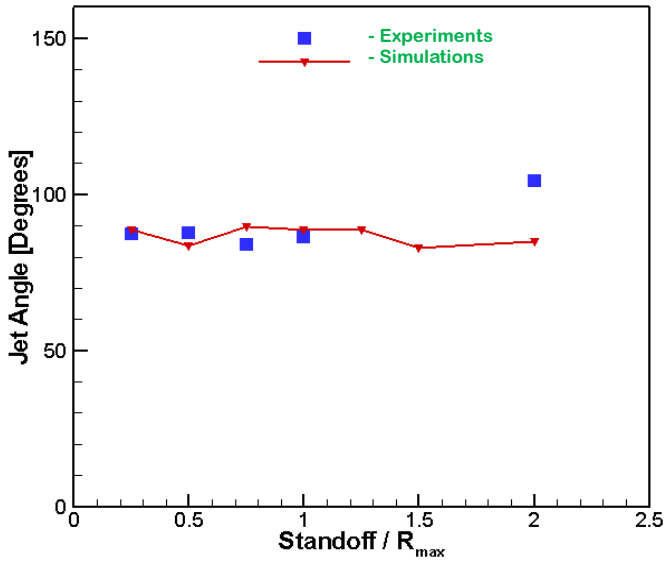

Figure 15.Variation of jet angle for various standoff distances.

The simulation conditions are: R_0= 1.17 cm, R_{max}= 16.48 cm, D = 121.92 cm and P_{atm} = 101230 Pa.

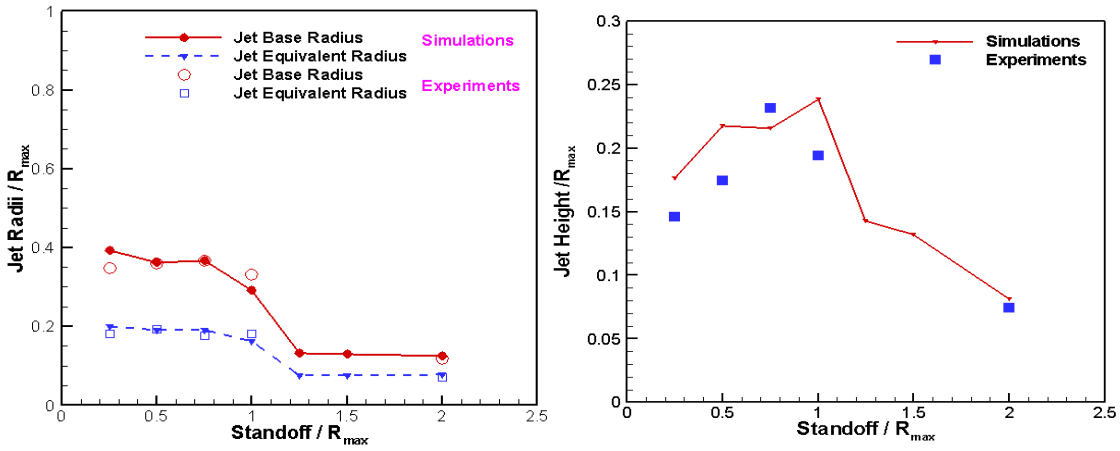

Figure 16. Normalized curves of variation of jet radii and jet height for various standoff distances.

The simulation conditions are: R_0= 1.17 cm, R_{max}= 16.48 cm, D = 121.92 cm, and P_{atm} = 101230 Pa.

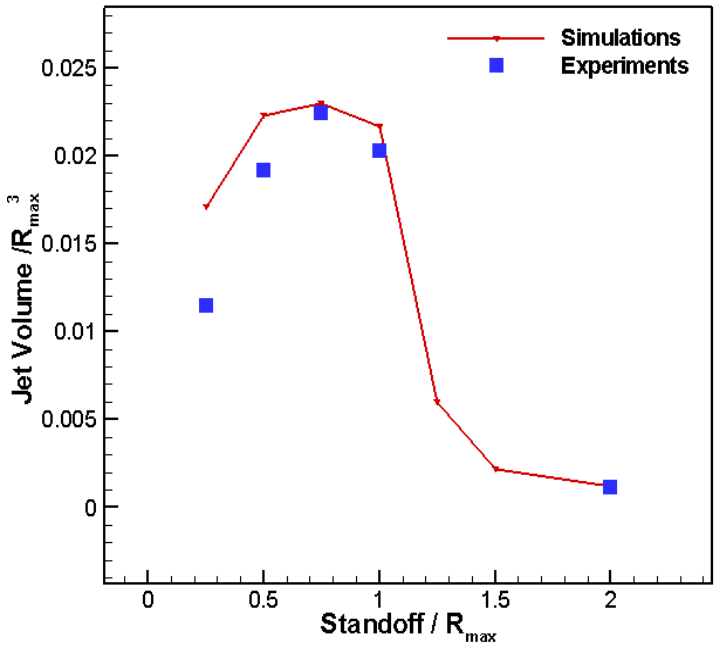

Figure 17. Normalized curves of variation of jet volume for various standoff distances.

The simulation conditions are: R_0= 1.17 cm, R_{max}= 16.48 cm, D = 121.92 cm and P_{atm} = 101230 Pa.

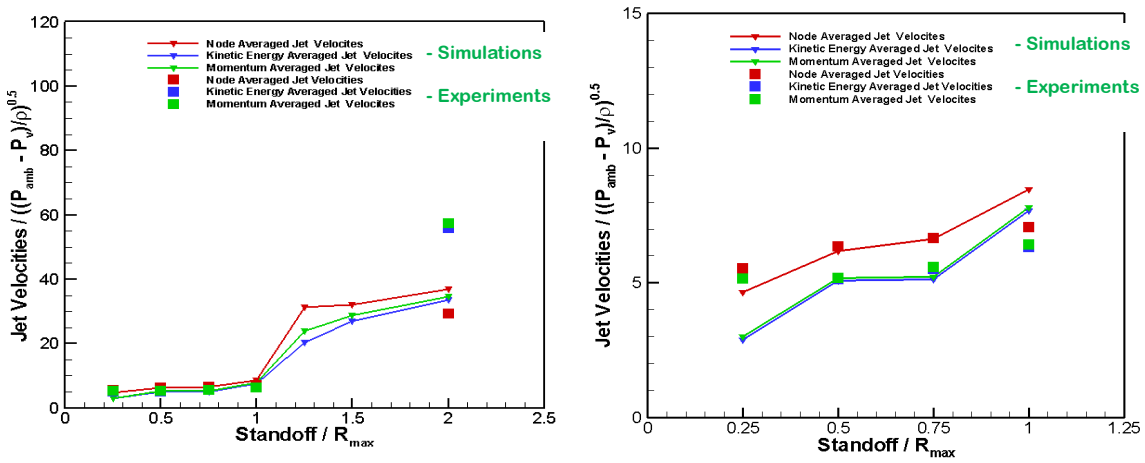

Figure 18. Normalized curves of variation of Jet Averaged Velocities for various Stand-off distances. The simulation conditions are: R_0= 1.17 cm, R_{max}= 16.48 cm, D = 121.92 cm and P_{atm} = 101230 Pa.

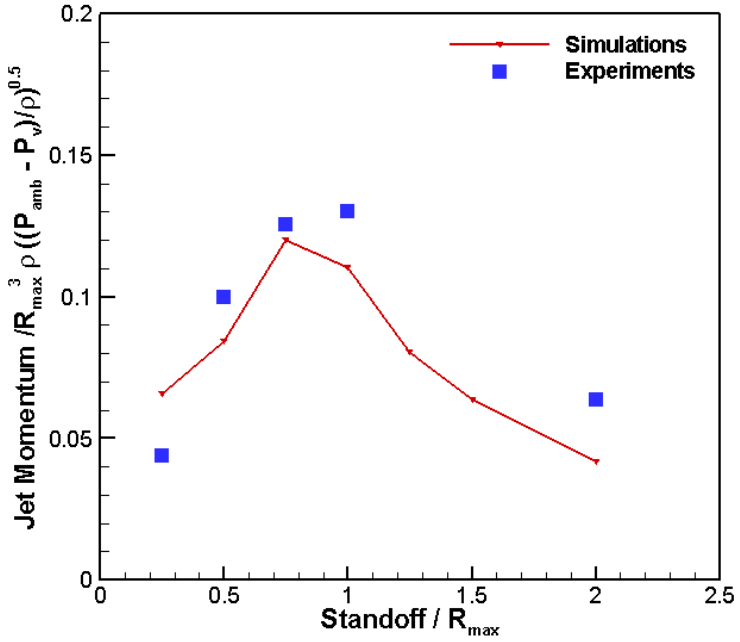

Figure 19. Normalized curves of variation of Jet Momentum for various Stand-off distances. The simulation conditions are: R_0= 1.17 cm, R_{max}= 16.48 cm, D = 121.92 cm and P_{atm} = 101230 Pa.

CONCLUSIONS

In this study, we have conducted a number of simulations and scaled spark experiments in order to investigate the behavior of dynamic bubbles near a vertical wall and between a free surface and a bottom.

From the 3D numerical simulations of the bubble dynamics near a vertical wall, confirmed with the spark tests, we deduced the jet characteristics as function of standoff distance.

The trends of the jet parameters curves (under the studied conditions) indicate a strong dependence on the standoff distance from the wall. For the region of interest where damage at the wall can occur the jet equivalent radius did not vary significantly with the standoffs. However, the jet volume changes strongly with the standoff. This results in an optimum standoff distance to maximize the momentum contained in the reentrant jet.

Finally, very good comparisons between the spark tests and the 3DYNAFS-BEM© simulations at the two simulated scales (spark tests and larger-scale), confirms again that numerical simulations and the use of laboratory spark tests scale experiments can be a very useful tools to investigate bubble/wall interactions and predictions.

REFERENCES

1. Jayaprakash, A., Chahine, G. L., and Hsiao, C-T., " Numerical and Experimental Study of the Interaction of a Spark Generated Bubble and a Vertical Wall", IMECE2010-40515, ASME 2010 International Mechanical Engineering Congress & Exposition, Vancouver, British Columbia, November 10-12, 2010.
2. Chahine, G. L., Prabhukumar, S., and Duraiswami, R., "Bubble Dynamics near A Cylindrical Body: 3-D Boundary Element Simulation of the ONR Snay/Goertner Bubble Benchmark Problem", 67th Shock and Vibration Symposium, Monterey, CA November 1996.
3. Chahine, G. L. and Duraiswami, R., “Dynamical Interactions in a Bubble Cloud”, Journal of Fluids Engineering, Vol.114, p.680, 1992.
4. Rayleigh, L., “On the pressure developed in a liquid during the collapse of a spherical cavity”, Phil. Mag. 34, 94-98, 1917.
5. M. Plesset, “The dynamics of cavitation bubbles”, ASME Journal of Applied Mechanics 16, 228-231, 1949.
6. Ellis, A. T., “Parameters Affecting Cavitation and Some New Methods for Their Study,” California Institute of Technology, Rep E-115.1, 1965.
7. Kling, C. L., “A High Speed Photographic Study of Cavitation Bubble Collapse,” *Ph.D. thesis*, University of Michigan, Ann Arbor, 1970.

8. Lauterborn, W. and Bolle, H., "Experimental investigations of cavitation-bubble collapse in the neighborhood of a solid boundary", Journal of Fluid Mechanics, vol. 72, p.391-399, 1975.
9. Chahine, G. L., “Etude Locale du Phénomène de Cavitation Analyse des Facteurs Régissant la Dynamique des Interfaces,” Docteur ès Sciences Thesis, Université Paris VI, 1979.
10. Chahine, G.L. and Bovis, A., "Oscillation and Collapse of a Cavitation Bubble in the Vicinity of a Two Liquid Interface", Cavitation and Inhomogeneities in Underwater Acoustics, Springer-Verlag ed. New York, pp. 23-29, 1980.
11. Bovis, A.G. and Chahine. G.L., "Asymptotic Study of the Non-Spherical Collapse of a Bubble Near a Solid Wall", ASME Cavitation and Polyphase Flow Forum; pp. 14-18, New Orleans, LO, 1980.
12. Bovis, A.G. and Chahine, G.L., "Etude Asymptotique de l'Interaction d'une Bulle Oscillante avec une Surface Libre Voisine", Journal de Mécanique, Vol. 20 No. 3, pp. 537-556, 1981.
13. Blake, J. R. and Gibson, D. C., "Cavitation Bubbles near Boundaries", Annual Review of Fluid Mechanics, Vol. 19: 99-123, 1987.
14. Shima A. and Tomita, Y., ‘‘Some Numerical Aspects of Cavitation Bubble Collapse,’’ in Annual Review of Numerical Fluid Mechanics and Heat Transfer, edited by L. A. Dziobek and B. Brienza ~Hemisphere, Washington, DC, Vol. 2, Chap. 5, pp. 198–226., 1989.
15. Blake, J. R., Taib, B. B. and Doherty G., “Transient cavities near boundaries. Part 1. Rigid boundary”, Journal of Fluid Mechanics, 170, 479-497, 1986.
16. Lindau, R. and Lauterborn. W., "Cinematographic observation of the collapse and rebound of a laser-produced cavitation bubble near a wall", Journal of Fluid Mechanics, 479,327-348, 2003.
17. Ohl, C.-D., Philipp, A. and Lauterborn, W., "Cavitation bubble collapse studied at 20 million frames per second", Ann. Phys., Volume 507, Issue 1, pages 26-34, 1995.
18. Isselin, J-C., Alloncle, A-P., and Autric, M., "On laser induced single bubble near a solid boundary: Contribution to the understanding of erosion phenomena, Journal of Applied Physics, 84, 5766, 1998.
19. Popinet S., and Zaleski S., "Bubble collapse near a solid boundary: a numerical study of the influence of viscosity", Journal of Fluid Mechanics, 464, pp 137-163, 2002.
20. Klaseboer, E., Hung, K. C., Wang, C., Wang, C. W., Khoo, B. C., Boyce, P., Debono, S. and Charlier H., "Experimental and numerical investigation of the dynamics of an underwater explosion bubble near a resilient/rigid structure", Journal of Fluid Mechanics, 537 , pp 387-413, 2005.

21. Van Der Geld, C. W. M. and Kuerten, J. G. M., "Axisymmetric dynamics of a bubble near a plane wall", Journal of Fluid Mechanics , 640: 265-303, 2009.
22. Zhang, A.M., Yao, X.L., and Feng, L.H., "The dynamic behavior of a gas bubble near a wall", Ocean Engineering, Volume 36, Issues 3-4, Pages 295-305, 2009.
23. Johnsen, E., and Colonius, T., "Numerical simulations of non-spherical bubble collapse", Journal of Fluid Mechanics, 629: 231-262, 2009.
24. E.A. Brujan, A. Vogel – Stress wave emission and cavitation bubble dynamics by nanosecond optical breakdown in a tissue phantom. Journal of Fluid Mechanics, 558, 281-308, 2006
25. Chahine, G.L., and Harris. G.H., "Development and Validation of a Multicycle Bubble Model for Explosion Applications", 68th Shock Vibration Symposium, Hunt Valley, Maryland, 1997.
26. Cook, J. A., Gleeson, A. M., Roberts, R. M. and Rogers. R. L.,"A spark-generated bubble model with semi-empirical mass transport", J. Acoust. Soc. Am. Volume 101, Issue 4, pp. 1908-1920, 1997.
27. Chahine, G. L., Duraiswami, R., and Lambrecht, C.J., “A method for validation of Underwater Explosion Bubble Codes: The Use of Benchmark Observations for Spark Generated Bubbles”, Dynaflow Inc. Technical Report *6.002-18*, June 1994.
28. Chahine, G. L., Frederick, G. S., Lambrecht, C., Mair, H. and Harris, G. S., “Spark-generated bubbles as laboratory-scale models of underwater explosions and their use for validation of simulation tools,” *SAVIAC* Proceedings of the 66th Shock and Vibrations Symposium, Volume I, Biloxi, MS, 1995.
29. Chahine, G. L., and Hsiao, C.-T., " 3DYNAFS© - A Three-Dimensional Free Surface and Bubble Dynamics Code", User manual version 7-086, Feb 2010.
30. Chahine. G. L., Annasami. R., Hsiao, C-T., and Harris, G., "Scaling rules for the prediction of UNDEX bubble Re-Entering Jet Parameters", Journal of Critical Technologies in Shock & Vibration, December 19, 2002.
31. Choi, J., Hsiao, C-T., Chahine, G. L., and Ceccio, S., "Growth, Oscillation and Collapse of Vortex Cavitation Bubbles", Journal of Fluid Mechanics, Vol 624, pp 255-279, April 2009.
32. Chahine GL, Duraiswami R. Method for calculating 2-D and 3-D underwater explosion bubble behavior in free water and near structures. NSWC Dahlgren Division Report NSWCDD/TR-93/44 (limited distribution), 1993.

33. Chahine GL, Duraiswami R, Kalumuck KM, Boundary element method for calculating 2-D and 3-D underwater explosion bubble loading on nearby structures including fluid-structure interaction effects. NSWC Dahlgren Div. Rpt. NSWCDD/TR-93/46 (limited distribution), 1997.
34. Chahine G.L., Prabhukumar, S. and Duraiswami, R., Bubble Dynamics Near a Cylindrical Body: 3-D Boundary Element Simulation of the ONR/SNAY Goertner Bubble Benchmark Problems, 67th Shock & Vibration Symposium, Vol. 2, San Diego, CA, 1996.
35. Chahine, G. L. Hsiao, C.-T. and Kalumuck, K. M., "Simulation of Surface Piercing Body Coupled Response to Underwater Bubble Dynamics Utilizing 3DynaFS, a Three Dimensional BEM Code", Computational Mechanics, Springer-Verlag, Vol. 32, No. 4-6, pp 319-326, December 2003.
36. Chahine, G. L., and Kalumuck, K.M., "BEM Software for Free Surface Flow Simulation Including Fluid-Structure Interaction Effects", International Journal of Computer Applications in Technology, Vol. 11, No. 3/4/5, 1998.
37. Chahine, G. L., and Kalumuck, K., “BEM Software for Free Surface Flow Simulation Including Fluid Structure Interaction Effects,” International Journal of Computer Application in Technology, Vol. 3/4/5, 1998.
38. Kalumuck, K. M., Duraiswami, R., and Chahine, G. L. “Bubble Dynamics Fluid-Structure Interaction Simulation on Coupling Fluid BEM and Structural FEM Codes”, Journal of Fluids and Structures, 9, pp. 861-883, 1995.
39. Kalumuck, K. M., Duraiswami, R. and Chahine, G. L., “Analysis of the Response of a Deformable Structure to Underwater Explosion Bubble Loading Using a Fully Coupled Fluid-Structure Interaction Procedure”, *SAVIAC* Proceedings of the 66th Shock and Vibration Symposium, Volume I, Biloxi, MS, 1995.
40. J.R. Krieger and G. L. Chahine, “Acoustic signals of underwater explosions near surfaces”, Journal Acoustic Society of America, Vol.118, pp. 2961-2974, November 2005.